QoT-Aware Performance Evaluation of Spectrally-Spatially Flexible Optical Networks over FM-MCFs

FARHAD ARPANAEI[1], NAHID ARDALANI[1,*], HAMZEH BEYRANVAND[2], AND BEHNAM SHARIATI[3]

[1] Department of Electrical Engineering, Central Tehran Branch, Islamic Azad University, Tehran, Iran
[2] Department of Electrical Engineering, Amirkabir University of Technology, Tehran, Iran
[3] was with the Universitat Politecnica de Catalunya (UPC), and is now with Fraunhofer HHI, Berlin, Germany
[*] Corresponding author:nardalani96@gmail.com

Compiled June 29, 2020

In this paper, we study the quality of transmission (QoT) aware routing, modulation level, and resource assignment (RMRA) problem for transparent flexible optical networks (FONs) over few-mode multi-core fibers (FM-MCFs). We consider two three-dimensional resource assignment (3DRA) algorithms, named liberal and conservative, that are compatible with fractional joint switching (FrJ-Sw). The three resource dimensions are core, mode, and spectrum. Furthermore, we analyze two modulation-level selection (MLS) algorithms (one on-line and one off-line), and three path selection algorithms (favoring shortest path, best balanced load or highest QoT). The results show that the liberal 3DRA algorithm has a similar blocking probability (BP) as compared to conservative 3DRA. However, performance metrics such as computation time, optical signal-to-noise ratio (OSNR), and number of required lasers are all improved with conservative 3DRA. Moreover, the BP decreases and the average OSNR increases by applying the on-line MLS algorithm as compared to the off-line algorithm. Finally, we use an on-line liberal algorithm with a path selection policy that favors load balancing to generate a solution with the lowest BP.

http://dx.doi.org/10.1364/ao.XX.XXXXXX

1. INTRODUCTION

IP traffic keeps growing exponentially due in part to bandwidth-hungry applications such as on-line gaming, remote learning, telemedicine, and Internet of Things (IoT) applications. Overall IP traffic is expected to grow to 396 Exabytes (EB) per month by 2022, up from 122 EB per month in 2017, i.e., a compound annual growth rate of 26% [1]. Space-division multiplexing (SDM) has been introduced as a promising solution to overcome the eventual capacity crunch due to the ever-increasing traffic [2]. Indeed, SDM technology can be exploited together with flexible optical networking to realize the SDM-FON paradigm [3]. In FONs, characteristics such as modulation level, symbol rate, forward error correction (FEC) overhead, and sub-carrier bandwidth are continuously adapted to the traffic demands [4]. Indeed, FONs enable the construction of spectrum-efficient "super-channels (Sp-Chs)," which consist of several densely packed sub-channels, offering tunable bit rates from a few tens of Gigabit per second (Gbps) to the Terabit per second (Tbps) range [4]. Moreover, flexible and programmable transponders and switches are utilized for the transmission, switching, and reception of such Sp-Chs, so that efficient resource utilization is preserved as the traffic changes. Further performance improvement of SDM-FONs can be achieved with the capabilities offered by programmability and software-defined networking (SDN) [2, 5]. In SDM-FONs, each connection is allocated one or more frequency slots in each subspace, e.g., cores in multi-core fibers (MCFs), modes in few-mode fibers (FMFs), or modes and cores in FM-MCFs, and is assigned a suitable modulation level, which is determined based on the acceptable QoT criteria and the end-to-end optical reach [6].

FM-MCFs can substantially improve the fiber capacity in SDM networks; however, the cumulative impact of physical layer impairments (PLIs) introduced among the cores and modes of such fibers can significantly affect the QoT of the signals [7]. Nevertheless, multi-input and multi-output (MIMO) digital signal processing at the receiver can compensate for most of the destructive linear impairments at the expense of higher cost and computational complexity of transceivers [8].

From the network design point of view, by exploiting the flexibility, programmability, and reconfigurability of bandwidth variable transponders in SDN-based FONs, one can reduce the MIMO processing at the transceivers by managing the PLIs

[9]. Indeed, physical layer monitoring for cross-layer design is essential to realize a cognitive SDN-based SDM-FON [10]. In other words, physical layer feedback can contribute to the performance improvement of the network by allowing the selection of the most appropriate symbol rate, FEC, and modulation level [4, 11]. To this end, we propose several dynamic on-line QoT-aware RMRA algorithms for SDM-FONs over FM-MCFs. In these algorithms, the modulation level is adaptively selected at the time of connection establishment based on the QoT.

A. Prior Work and Contributions

Unlike FONs, which deal with routing and spectrum assignment (RSA), SDM-FONs must address routing, spectrum, and space assignment (RSSA) [12]. Various schemes and algorithms, including integer linear programming (ILP)/mixed ILP (MILP) and heuristic approaches to RSSA have been evaluated in previous work [3, 13–16]. In particular, Klinkowski *et al.* published a comprehensive survey of many RSSA algorithms for SDM-EONs in [17]. In that survey, various SDM media, such as MCFs, FMFs, and FM-MCFs, and several static and dynamic RSSA algorithms were considered.

One of the earliest works to address spectrum and space assignment methods for FM-MCFs is [18]. However, it did not consider PLIs, such as inter- and intra-mode crosstalk (IrM-XT and IaM-XTs) and inter-core crosstalk (IC-XT). On the other hand, the authors in [19] considered these PLIs in a machine learning-based approach to RSSA, but with two-dimensional resource assignment.

Regarding SDN-enabled spectral and spatial FONs, the authors in [5] presented and experimentally investigated the first SDN-controlled sliceable SDM-wavelength division multiplexing (WDM) transceiver architecture to support multiple and independent SDM Sp-Chs in parallel, enabling effective use of the spatial and spectral resources. Their approach considered SDM Sp-Chs of variable size, where the capacity of the Sp-Chs is increased or decreased by using the spatial modes. Furthermore, they proposed a heuristic RSSA and an SDN-controlled SDM network architecture that implements adaptive few-mode SDM transmitters and SDM MIMO receivers controlled by SDN where the modulation format, the size of the MIMO matrix, and the number of taps are dynamically adapted to the modes of the Sp-Chs.

Our main contributions in this paper are described next. Unlike previous work on RSSA for SDM optical networks over FM-MCFs, e.g., [18, 19], we propose several comprehensive dynamic online 3D-RMRA algorithms based on a closed-form formula for OSNR for FM-MCFs by analyzing all 3DRA schemes compatible with FrJ-Sw. We focus on the flexibility of selecting modulation levels based on the transmission distance and QoT for an SDN-controlled SDM-FON over FM-MCF and present a network-wide performance evaluation. Furthermore, extending our previous work [20], which investigated PLIs in FM-MCFs, here, we propose two dynamic 3D QoT-aware RMRA algorithms. One is based on post-QoT computation (QC) and the other is based on pre-QC. Furthermore, we propose an on-line scheme where the modulation level can be adaptively selected when a connection is first established, based on the transmission distance and QoT degradation due to PLIs such as IrM-XTs, IaM-XTs, and IC-XT.

The rest of this paper is organized as follows. The system model and main assumptions are presented in Section 2. This includes a description of the QoT estimator. We develop a comprehensive analysis of 3DRA compatible with FrJ-Sw over FM-MCFs in Section 3. This includes descriptions of liberal and conservative 3DRA, as well as the assumed architecture of the transceivers. We extend the analysis to two 3D QoT-aware RMRA algorithms in Section 4, called pre-QC and post-QC, followed by numerical analysis and simulation results in Section 5. Finally, we conclude in Section 6.

A list of the variables and notation used throughput the paper is presented in Table 1.

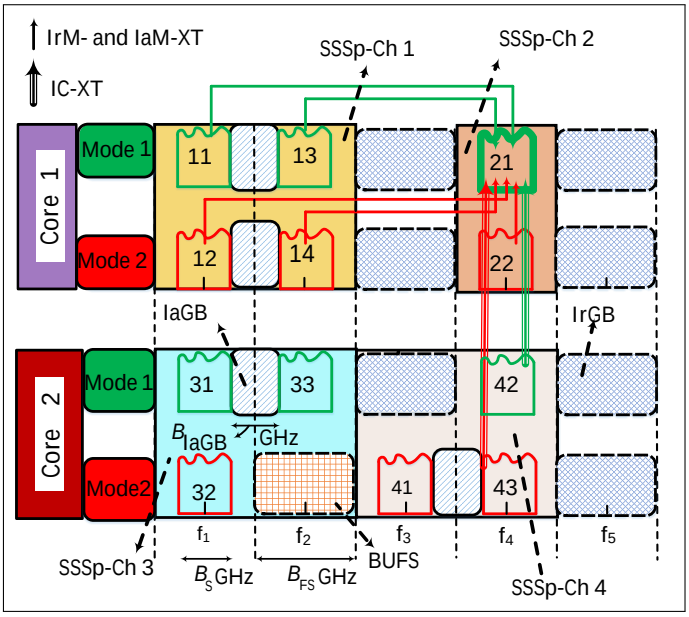

Fig. 1. A conceptual illustration of physical layer interactions among cores, modes, and frequency slots over FM-MCFs with weakly-coupled modes and uncoupled cores, assuming two cores, two modes, and five frequency slots. Label rx stands for x^{th} Sb-Ch of connection r.

2. SYSTEM MODEL

We consider a 3D SDM-FON system based on a spectral/spatial super-channel (SSSp-Ch) scheme to model transmission over FM-MCFs in the FrJ-Sw regime [21–23]. In the proposed 3D SDM-FON SSSp-Ch, the requested bandwidth of a high bit-rate connection request is transformed to multiple lower bit-rate sub-channels (Sb-Chs) compatible with finer programmable and sliceable bandwidth variable transponders (SBVTs).

It should be noted that the bit rate of a Sb-Ch is selected according to the transmission reach, and adaptively selected based on QoT on-line feedback by utilizing programmable and flexible SBVTs. By considering the FrJ-Sw regime, each connection is assigned to the idle FSs of one or more modes belonging to a core [5, 22]. For example, as depicted in Fig.1 for an FM-MCF with two modes and two cores, the Sb-Chs of each connection can be distributed across two modes of a core. The Sb-Chs located on the first and second modes are colored by green and red, respectively. Connection 1, which constitutes SSSp-Ch 1, is carried by four Sb-Chs, i.e., 11, 12, 13, and 14. Each Sb-Ch occupies one FS in Fig.1.

It is worth mentioning that the required FSs for each Sb-Ch are determined according to the symbol rate and the modulation format of the transceivers. For example, when the transceivers operate at a fixed baud rate of 32 Gbaud as discussed in [24], a Nyquist-WDM (N-WDM) Sb-Ch occupies 37.5 GHz or three FSs (assuming 12.5 GHz per FS), whereas, in the proposed model

Table 1. Variables and Notation.

Symbol	Description
$\mathcal{C}$	a set of cores in each FM-MCF link.
$\mathcal{M}$	a set of modes in each core.
$\mathcal{F}$	a set of frequencies in each mode.
$\mathcal{S}$	a set of FSs in each FM-MCF link.
$\mathcal{R}$	a set of connection (lightpath) requests.
$G(\mathcal{N},\mathcal{L})$	the network topology.
$\mathcal{N}$	the set of nodes.
$\mathcal{L}$	the set of undirected FM-MCF links.
$\mathcal{L}^{r,k}$	a set of network links dedicated to the k^{th} path of connection r.
T^s	the tuple of s^{th} FS on mode m, frequency f, and core c.
$R^r = (N_S^r, N_D^r, \rho^r)$	a connection request tuple with source node N_S^r, destination node N_D^r, and bit rate ρ^r (Gbps).
d^k	distance of k^{th} candidate path (km).
$d_{\max}$	maximum reach associated with the modulation level (km).
n_{FS}^r	number of FSs for r^{th} connection.
n_{Sb}^r	number of Sb-Chs for r^{th} connection.
Δ_{FS}	number of FSs for each Sb-Ch.
Υ^r	modulation level number for r^{th} connection.
$Q_{th}^{\Upsilon^r}$	QoT threshold for r^{th} connection with modulation level Υ^r.
$\pi^{T^s,r,k}$	the state value of an FS on tuple T^s in k^{th} path for connection r.
$\omega^{T^s,r,l}$	the state value of an FS on tuple T^s in link l, dedicated to the connection r.
B_{Sb}	Sb-Ch bandwidth (GHz).
B_{FS}	Channel spacing bandwidth (GHz).
$\boldsymbol{LST}^l$	link state tensor for l^{th} link.
$\boldsymbol{PST}^{r,k}$	k^{th} path state tensor for r^{th} connection.
$\boldsymbol{P}^r$	path vector of connection r.
$\boldsymbol{FS}^r$, $\boldsymbol{IrGB}^r$, and $\boldsymbol{BUFS}^r$	allocated FSs, IrGBs, and BUFSs matrices for connection r, respectively.
$[\ ]$	empty matrices/tensors.

in [25], each multi-band orthogonal frequency division multiplexing (MB-OFDM) Sb-Ch occupies one FS. The concept of MB-OFDM and N-WDM Sp-Ch solutions for FONs was first published in [25]. In [26], the authors experimentally evaluated flexible optical switching solutions with ultra-narrow spectral granularity, using the proposed all-optical end-to-end transport of an Sp-Ch over SMFs in [25]. The proposed optical cross-connects for high bit-rate FONs utilize fine spectral resolution filtering elements, thus allowing individual Sb-Chs to be added to/dropped from an Sp-Ch. This provides flexibility in optical transport networks through the adaptability of the network resources to the traffic requests. As shown in [25], another vital benefit of the proposed SSSp-Ch scheme is the ability to optimize the all-optical grooming process in multi-layer networks (from the optical layer up to the IP layer). This leads to notable cost savings and reduced energy consumption compared to an electronic (e.g., Optical Transport Network (OTN)) based aggregation approach.

In this paper, we extend the proposed all-optical traffic grooming solution to SDM-FONs over FM-MCFs by utilizing the ultra-narrow granularity of the wavelength selective switches (WSSs) proposed in [27] and SDM reconfigurable optical add-drop multiplexers (ROADMs) described in [22, 28]. The use of ultra-fine optical cross-connects allows the add/drop of individual Sb-Chs .

A. System Level Assumptions

A.1. Physical Layer Interactions

Similar to [20] and [29], we assume FM-MCFs with weakly-coupled mode-multiplexed transmission over uncoupled cores. With this assumption, the IrM-XT, IaM-XT, and IC-XT imposed by other Sb-Chs on the Sb-Ch labeled 21 are illustrated in Fig.1. IC-XT is one of the most important impairments of uncoupled MCFs.

According to [30] (theoretical aspects) and [31] (experimental aspects), because the nonlinear interference (NLI) noise has been verified to be like a Gaussian noise source, independent of amplified spontaneous emission (ASE) noise, the statistical IC-XT can be treated as another Gaussian noise source, independent of ASE and nonlinear noise. Accordingly, the modified OSNR model for uncoupled MCFs (or weakly coupled MCFs [32, 33]) can be obtained from $\frac{P_{tx,ch}}{P_{ASE}+P_{NLI}+P_{IC\text{-}XT}}$, where $P_{tx,ch}$ is signal power, P_{ASE} is ASE noise power, P_{NLI} is NLI noise power, and $P_{IC\text{-}XT}$ is IC-XT. Indeed, in [30] by using a coupled-core approach for uncoupled MCFs, it was shown that the spatial distribution of the electric field propagating in one core is not affected by the presence of other cores. Therefore, with these design assumptions, nonlinear IC-XT can be considered negligible.

Lastly, we consider the weak-coupling regime for NLIs in each core, according to Ref.[34]. In order to apply the GN-model, we assume that the input signal is Gaussian, and the NLIs are statistically independent of both the ASE noise and the transmitted signal. Also, we neglect the mode-dependent loss as in [34].

A.2. Analytic Environment

We define the analytic environment for our system model and define the variables used in our proposed algorithms. In the system model, the spectral granularity for the MB-OFDM/N-WDM Sb-Chs is equivalent to a spectral slot of bandwidth $B_{Sb} = \Delta_{FS} \times B_{FS}$ GHz and can be grouped to constitute an SSSp-Ch transporting high bit rates such as 100, 200, 400, or 1000 Gbps, where Δ_{FS} is the required number of FSs of each Sb-Ch. The intra-guardband (IaGB) between the Sb-Chs requires B_{IaGB} GHz for the MB-OFDM waveform (see Fig.1). Moreover,

Core	Mode	Frequency Slot		
		1	2	3
1	1	T^1=(1,1,1)	T^4= (1,2,1)	T^7= (1,3,1)
	2	T^2= (2,1,1)	T^5= (2,2,1)	T^8= (2,3,1)
	3	T^3= (3,1,1)	T^6= (3,2,1)	T^9= (3,3,1)
2	1	T^{10}= (1,1,2)	T^{13}= (1,2,2)	T^{16}= (1,3,2)
	2	T^{11}= (2,1,2)	T^{14}= (2,2,2)	T^{17}= (2,3,2)
	3	T^{12}= (3,1,2)	T^{15}= (3,2,2)	T^{18}= (3,3,2)

Fig. 2. FS order in a LST with 18 FSs for a link with 3 modes, 3 frequencies, and 2 cores according to the first-fit CFM search priority scheme.

as shown in Fig.1, we assume B_{FS} GHz is required for the inter-guardband(IrGB) and for the busy unused FSs (BUFS). The BUFS arise due to FrJ-Sw in the intermediate nodes, essentially leading to stranded spectrum.

The input of our algorithms is a graph $G = (\mathcal{N}, \mathcal{L})$, where $\mathcal{N}$ is a set of optical nodes, and $\mathcal{L}$ is a set of FM-MCF links. The set of connections is represented by $\mathcal{R}$. For the l^{th} link, the link state is defined as a 3D tensor called link state tensor (LST), $\boldsymbol{LST}^l$, where $l \in \mathcal{L}$. Each $\boldsymbol{LST}^l$ has $|\mathcal{M}| \times |\mathcal{F}| \times |\mathcal{C}|$ elements (or FSs), and each FS can be idle or busy. The elements of $\boldsymbol{LST}^l$ are represented by $\omega^{T^s,r,l}$, i.e., the FS situated in mode m, frequency f, and core c on link l for connection r. The tuple $T^s = (m, f, c)$ denotes the position of each FS (see Fig.2), where $s \in \mathcal{S} = \{1, 2, 3, \ldots, |\mathcal{S}| = |\mathcal{M}| \times |\mathcal{F}| \times |\mathcal{C}|\}$ (set of FSs). Lastly, it should be noted that the order of tuples is related to the search priority that will be discussed in detail in Section 3. For example, as shown in Fig.2, the CFM search priority is performed in order of mode (M), frequency (F), and core (C).

B. QoT Estimator for FM-MCFs

According to [35] the end-to-end OSNR of a Sb-Ch for connection r on the tuple $T^s = (m, f, c)$ in the k^{th} path with I^l spans is given by

$$OSNR^{T^s,r,k}_{\text{Total}} = \left(\sum_{l=1}^{|\mathcal{L}^{r,k}|} \sum_{i=1}^{I^l} \frac{1}{OSNR^{T^s,r,l,i}} \right)^{-1} \quad \textbf{(1)}$$

where the corresponding SNR is obtained from $SNR^{T^s,r,k} = \frac{B_{\text{ref}}}{R_{\text{sym}}} OSNR^{T^s,r,k}_{\text{Total}}$ [36]. (We define a span as the portion of the fiber between amplifier sites.) R_{sym}, B_{ref}, and $\mathcal{L}^{r,k}$ are the symbol rate, the noise bandwidth, and the set of network links utilized by path k of connection r, respectively. Furthermore, according to the discussion in sub-section A.1, and considering the PLI analysis of SDM fibers in [34] and [36], especially for weakly-coupled few modes over uncoupled multi-core fibers [29], we can introduce a QoT estimator according to the OSNR of each Sb-Ch of connection r on span i from link l with bandwidth $B^{T^s,r,l,i}$ with the Sb-Ch frequency center (v^{T^s}) located at tuple T^s:

$$OSNR^{T^s,r,l,i} = \frac{P^{T^s,r,l,i}_{\text{tx}}}{P^{T^s,l,i}_{\text{ASE}} + P^{T^s,r,l,i}_{\text{IrM\&IaM-XT}} + P^{T^s,r,l,i}_{\text{IC-XT}}} \quad \textbf{(2)}$$

$P^{T^s,l,i}_{\text{ASE}} = n_{\text{F}} h v^{T^s} (e^{\alpha L^{l,i}} - 1) B_{\text{ref}}$ is the noise power caused by the Erbium doped fiber amplifier (EDFA) and $P^{T^s,r,l,i}_{\text{tx}}$ is the transmitted power of the corresponding Sb-Ch. Moreover, $n_{\text{F}}, h, \alpha, and L^{l,i}$ are the noise figure, Plank's coefficient, attenuation coefficient, and span length, respectively. Without loss of generality, we assume that all links have the same physical layer parameters, i.e., loss, dispersion, and NLI coefficients. Moreover, the NLIs including IrM-XT and IaM-XT power, and IC-XT power according to a linear formula for estimating IC-XT [37], can be calculated from Eq. (3) and Eq. (4), respectively:

$$P^{T^s,r,l,i}_{\text{IrM\&IaM-XT}} = G^{T^s,r,l,i}_{\text{IM-XT}} B^{T^s,r,l,i} \quad \textbf{(3)}$$

$$P^{T^s,r,l,i}_{\text{IC-XT}} = \sum_{r' \neq r, r' \in \mathcal{C}} \sum_{m \in \mathcal{M}} \mu^{l,i}_{\text{IC-XT}} P^{T^s,r,l,i}_{\text{tx}} \quad \textbf{(4)}$$

Without loss of generality, we assume the SBVTs have a fixed symbol rate, hence, the required bandwidth of each Sb-Ch, i.e., $B^{T^s,r,l,i}$ is fixed in each span and link, and equals B_{Sb}. Additionally, the core coupling is calculated from $\mu^{l,i}_{\text{IC-XT}} = \frac{2\kappa^2 g}{\beta \Lambda} L^{l,i}$, where, κ, g, β, and Λ are coupling coefficient, bending radius, propagation constant, and core pitch, respectively. Furthermore, the power spectral density of IrM-XT and IaM-XT is obtained from Eq. (5), where $T^{s'} = (m, f', c)$, $T^{s''} = (m', f', c)$, $T^{s^*} = (m', f, c)$, $L^{l,i}_{\text{eff}} = \frac{1 - exp\{\alpha L^{l,i}\}}{\alpha}$, $L_{\text{eff,a}} = \frac{1}{\alpha}$, and γ, $G^{T^s,r,l,i}_{\text{tx}}$, $h^{T^s T^s}$, $h^{T^s T^{s^*}}$, and β_2 are nonlinear parameter, transmitted power spectral density, intra and inter nonlinear coupling coefficients, and average group velocity dispersion, respectively. Also, $\delta^{T^s T^{s'}}$ equals 1 when $f = f'$ and 0 otherwise. Finally, for simplicity, we assume fixed span lengths on all links and fixed launch power for all connections.

3. FRJ-SW RESOURCE ALLOCATION SCHEMES

A. Performance analysis of 3DRA schemes

There are four general 3DRA schemes to consider, namely single-mode single-core (SMSC), multi-mode single-core (MMSC), single-mode multi-core (SMMC), and multi-mode multi-core (MMMC). These schemes refer to the flexibility in assigning the FSs of a given SSSp-Ch, not the number of physical modes or cores. For example, in SMSC, all FSs of each SSSp-Ch must be distributed in one mode and one core. In MMSC, the FSs can occupy the FSs of several modes but in just one core. In SMMC, the FSs are allocated over one mode in several cores, and finally, in MMMC, there is no constraint on modes and cores for RA, and the FSs of a connection can be assigned to several modes and cores simultaneously. Furthermore, there are six possible permutations of first-fit RA policies in terms of search priority of frequency, mode, and core: CFM, CMF, MFC, MCF, FCM, and FMC. For example, the search priority in CMF is performed in order of frequency, mode, and core.

To illustrate these various schemes, we use the example of Fig.3, where we assume that three connections are requested with 2, 3, and 4 Sb-Chs, and each Sb-Ch occupies 3 FSs, i.e., $\Delta_{\text{FS}} = 3$. We assume that we are utilizing FM-MCF with 3 modes, 2 cores, and 12 FSs in each mode. We assume N-WDM waveforms for the SSS-SChs; thus, IaGBs are not needed. We define the effective spectrum utilization as $SU = \frac{\text{FSs convey information}}{\text{All busy FSs}}$. (Recall that FSs used for guard-bands or BUFSs are 'busy' FSs that do not convey information.) The resulting SU for each of the scenarios in Fig.3 is shown in the figure caption.

$$G_{\text{IM-XT}}^{T^s,r,l,i} = \frac{4}{3}\frac{\gamma^2}{|\mathcal{M}|^3}(L_{\text{eff}}^{l,i})^2 G_{\text{tx}}^{T^s,r,l,i}\left(\frac{4}{9}(h^{T^sT^s})^2\sum_{f'\in\mathcal{F}}(2-\delta^{T^sT^{s'}})\zeta^{T^sT^{s'}}(G_{\text{tx}}^{T^{s'},r,l,i})^2 + \sum_{m\neq m'\in\mathcal{M}}\sum_{f'\in\mathcal{F}}(h^{T^sT^{s^*}})^2(2-\delta^{T^sT^{s'}})\zeta^{T^sT^{s'}}(G_{\text{tx}}^{T^{s''},r,l,i})^2\right) \quad (5)$$

where,

$$\zeta^{T^sT^{s'}} = \frac{1}{4\pi|\beta_2|L_{\text{eff,a}}}\left(\texttt{asinh}(\pi^2|\beta_2|L_{\text{eff,a}}B_{\text{Sb}}(v^{T^s}-v^{T^{s'}}+\frac{B_{\text{Sb}}}{2})) + \texttt{asinh}(\pi^2|\beta_2|L_{\text{eff,a}}B_{\text{Sb}}(v^{T^{s'}}-v^{T^s}+\frac{B_{\text{Sb}}}{2}))\right)$$

(a) SMSC

Core	Mode	Frequency Slot 1	2	3	4	5	6	7	8	9	10	11	12
1	1	11			12			-1	0	0	0	0	0
	2	-2	-2	-2	-2	-2	-2	-1	0	0	0	0	0
	3	-2	-2	-2	-2	-2	-2	-1	0	0	0	0	0
2	1	21			22			23			-1	0	0
	2	-2	-2	-2	-2	-2	-2	-2	-2	-2	-1	0	0
	3	-2	-2	-2	-2	-2	-2	-2	-2	-2	-1	0	0

(b) MMSC

Core	Mode	Frequency Slot 1	2	3	4	5	6	7	8	9	10	11	12
1	1	11			-1	21			-1	0	0	0	0
	2	12			-1	22			-1	0	0	0	0
	3	-2	-2	-2	-1	23			-1	0	0	0	0
2	1	31			34			-1	0	0	0	0	0
	2	32			-2	-2	-2	-1	0	0	0	0	0
	3	33			-2	-2	-2	-1	0	0	0	0	0

(c) SMMC

Core	Mode	Frequency Slot 1	2	3	4	5	6	7	8	9	10	11	12
1	1	11			12			-1	21			-1	0
	2	-2	-2	-2	-2	-2	-2	-1	22			-1	0
	3	-2	-2	-2	-2	-2	-2	-1	23			-1	0
2	1	31			32			32			-1	0	0
	2	34			-2	-2	-2	-2	-2	-2	-1	0	0
	3	-2	-2	-2	-2	-2	-2	-2	-2	-2	-1	0	0

(d) MMMC-CMF

Core	Mode	Frequency Slot 1	2	3	4	5	6	7	8	9	10	11	12
1	1	11			-1	31			-1	0	0	0	0
	2	12			-1	32			-1	0	0	0	0
	3	-2	-2	-2	-1	33			-1	0	0	0	0
2	1	21			-1	34			-1	0	0	0	0
	2	22			-1	-2	-2	-2	-1	0	0	0	0
	3	23			-1	-2	-2	-2	-1	0	0	0	0

(e) MMMC-FCM

Core	Mode	Frequency Slot 1	2	3	4	5	6	7	8	9	10	11	12
1	1	11			12			-1	21			-1	0
	2	-2	-2	-2	-2	-2	-2	-1	23			-1	0
	3	-2	-2	-2	-2	-2	-2	-1	-2	-2	-2	-1	0
2	1	31			32			-1	22			-1	0
	2	33			34			-1	-2	-2	-2	-1	0
	3	-2	-2	-2	-2	-2	-2	-1	-2	-2	-2	-1	0

(f) MMMC-MCF

Core	Mode	Frequency Slot 1	2	3	4	5	6	7	8	9	10	11	12
1	1	11			-1	21			-1	31			-1
	2	12			-1	22			-1	32			-1
	3	-2	-2	-2	-1	23			-1	33			-1
2	1	0	0	0	0	0	0	0	0	34			-1
	2	0	0	0	0	0	0	0	0	-2	-2	-2	0
	3	0	0	0	0	0	0	0	0	-2	-2	-2	0

(g) MMMC-CFM

Core	Mode	Frequency Slot 1	2	3	4	5	6	7	8	9	10	11	12
1	1	11			-1	21			-1	31			-1
	2	-2	-2	-2	-1	23			-1	33			-1
	3	-2	-2	-2	-1	-2	-2	-2	-1	-2	-2	-2	0
2	1	12			-1	22			-1	32			-1
	2	-2	-2	-2	-1	-2	-2	-2	-1	34			-1
	3	-2	-2	-2	-1	-2	-2	-2	-1	-2	-2	-2	0

(h) MMMC-FMC

Core	Mode	Frequency Slot 1	2	3	4	5	6	7	8	9	10	11	12
1	1	11			-1	21			-1	31			-1
	2	-2	-2	-2	-1	23			-1	33			-1
	3	-2	-2	-2	-1	-2	-2	-2	-1	-2	-2	-2	0
2	1	12			-1	22			-1	32			-1
	2	-2	-2	-2	-1	-2	-2	-2	-1	34			-1
	3	-2	-2	-2	-1	-2	-2	-2	-1	-2	-2	-2	0

(i) MMMC-MFC

Fig. 3. Illustrative examples of first-fit 3DRA compatible with FrJ-Sw for all search priority schemes. The effective spectrum utilizations are shown in parentheses. (a): SMSC ($\frac{15}{51} = 29.4\%$), (b): MMSC ($\frac{27}{45} = 60\%$), (c): SMMC $\frac{15}{58} = 25.9\%$, (d): MMMC-CFM ($\frac{27}{63} = 42.9\%$), (e): MMMC-FCM ($\frac{27}{48} = 56.3\%$), (f): MMMC-MCF ($\frac{27}{66} = 40.9\%$),(g): MMMC-CMF ($\frac{27}{46} = 58.7\%$), (h): MMMC-FMC ($\frac{27}{70} = 38.6\%$),(i): MMMC-MFC ($\frac{15}{57} = 26.3\%$). Labels: 0 = idle, -1 = GB, -2 = BUFS, $rx = x^{th}$ Sb-Ch of connection r.

Since we cannot assign an FS in all modes of each core to more than one connection for FrJ-Sw 3DRA, the choice of first-fit search priority is not relevant in the 3DRA SMSC, MMSC, and SMMC scenarios. In Fig.3, with the SMSC and SMMC scenarios, connections 1 and 2 with 2 and 3 Sb-Chs respectively are established, whereas connection 3 with 4 Sb-Chs is blocked. All three connections are established in MMSC.

As should be obvious, the MMMC is the most flexible 3DRA scenario for FM-MCFs. However, it does not necessarily provide the best results in terms of effective spectrum utilization. For MMMC, we need to consider all six search priority schemes, as shown in (d) through (i) in Fig.3. All three connection requests are satisfied in each of the MMMC search priority schemes with the exception of connection 3 being blocked in MMMC-MFC. As noted above, MMSC also accommodates all three connections, but does so at a higher effective spectrum utilization as compared to any of the MMMC schemes (i.e., SU equals 60% and equals at most 59% in any of the MMMC scenarios). While this does not conclusively show that MMSC is better performing than MMMC in general, MMSC is simpler to implement. Moreover, first-fit CFM priority is the least time-consuming scheme for MMSC [22]. Thus, for the remainder of the paper, we focus on the MMSC-CFM scheme.

B. First-Fit MMSC-CFM 3DRA: Liberal v.s. Conservative

For first-fit MMSC-CFM, we propose two different 3DRA approaches, called liberal and conservative; see Algorithm 1 and Algorithm 2, respectively. The liberal and conservative 3DRA are established by applying two functions named LIBERAL and CONSERVATIVE, as described below.

First, let us describe the LIBERAL function in Algorithm 1. The inputs of the algorithm for connection r are the corresponding LSTs for all links of the k^{th} path, i.e., $\boldsymbol{LST}^l = [w^{Ts,r,l}]_{|\mathcal{M}|\times|\mathcal{F}|\times|\mathcal{C}|\times|\mathcal{L}^{r,k}|}; s \in \mathcal{S}, \forall\, l \in \mathcal{L}^{r,k} \subseteq \mathcal{L}$, the required number of FSs (n_{FS}^r), and the number of FSs for each Sb-Ch (Δ_{FS}). Note that the path k is obtained from the path selection algorithm that is discussed in Section 4. Additionally, we assume that $w^{Ts,r,l}$ is labeled 0 (in this case $r = 0$), -1, and -2 for the idle FSs, the IrGBs, and the BUFSs, respectively, and labeled 1 for busy FSs. Also, we need to define three two-dimensional matrices, i.e., $\boldsymbol{FS}^{r,l}$, $\boldsymbol{IrGB}^{r,l}$, and $\boldsymbol{BUFS}^{r,l}$ to insert the position of allocated FSs, IrGBs and BUFSs, respectively. The number of rows of these matrices equals n_{FS}^r, the number of IrGBs, and the number of BUFSs, respectively. Also, each matrix has three columns to insert corresponding mode, frequency, and core positions.

It is worth mentioning that we assume spectrum continuity and contiguity without mode and core change in the intermedi-

Algorithm 1. LIBERAL function

1: **procedure** LIBERAL($\boldsymbol{LST}^l$, n^r_{FS}, Δ_{FS}; $r \in \mathcal{R}, \forall l \in \mathcal{L}^{r,k}$)
2: Initializing:
3: $\boldsymbol{PST}^{r,k} \leftarrow \boldsymbol{LST}^l \circledast \boldsymbol{LST}^{l'} \circledast \cdots \circledast \boldsymbol{LST}^{|\mathcal{L}^{r,k}|}$,$q \leftarrow 0$
4: **while** $c \leq |\mathcal{C}|$ & $q < n^r_{\mathrm{FS}}$ **do**
5: $f \leftarrow 1$
6: **while** $f \leq |\mathcal{F}|$ & $q < n^r_{\mathrm{FS}}$ **do**
7: $y^r \leftarrow 0, q \leftarrow 0$,
8: $\boldsymbol{FS}^r \leftarrow [\,]$, $\boldsymbol{IrGB}^r \leftarrow [\,]$, and $\boldsymbol{BUFS}^r \leftarrow [\,]$
9: **while** $f \leq |\mathcal{F}|$ & $q < n^r_{\mathrm{FS}}$ & $\mathcal{A}$ & $\mathcal{B}$ **do**
10: **while** $m \leq |\mathcal{M}|$ & $q < n^r_{\mathrm{FS}}$ **do**
11: **if** $f < |\mathcal{F}|$ & $\pi^{T^s}|_{f+\Delta_{\mathrm{FS}}} \leq 0$ & $\mathcal{D}$ **then**
12: $\boldsymbol{FS}^r \leftarrow T^s|_{f\in\mathcal{D}}$, $q \leftarrow (q + \Delta_{\mathrm{FS}})$
13: $\boldsymbol{IrGB}^r \leftarrow T^s|_{f+\Delta_{\mathrm{FS}}}$,$y^r \leftarrow 1$
14: **else if** $f == |\mathcal{F}|$ & $\mathcal{D}$ **then**
15: $\boldsymbol{FS}^r \leftarrow T^s|_{f\in\mathcal{D}}$,$q \leftarrow (q + \Delta_{\mathrm{FS}})$,$y^r \leftarrow 1$
16: **else**
17: $\boldsymbol{BUFS}^r \leftarrow T^s|_{f\in\mathcal{D}}$
$m \leftarrow (m + 1)$
18: $f \leftarrow (f + \Delta_{\mathrm{FS}})$
19: $f \leftarrow (f + 1)$
20: $c \leftarrow (c + 1)$
21: **return** $\boldsymbol{FS}^r$, $\boldsymbol{IrGB}^r$,$\boldsymbol{BUFS}^r$,y^r

Algorithm 2. CONSERVATIVE function

1: **procedure** CONSERVATIVE($\boldsymbol{LST}^l$, n^r_{FS}, Δ_{FS}; $r \in \mathcal{R}, \forall l \in \mathcal{L}^{r,k}$)
2: Initializing:
3: $\boldsymbol{PST}^{r,k} \leftarrow \boldsymbol{LST}^l \circledast \boldsymbol{LST}^{l'} \circledast \cdots \circledast \boldsymbol{LST}^{|\mathcal{L}^{r,k}|}$,$q \leftarrow 0$
4: **while** $c \leq |\mathcal{C}|$ & $q < n^r_{\mathrm{FS}}$ **do**
5: $f \leftarrow 1$
6: **while** $f \leq |\mathcal{F}|$ & $q < n^r_{FS}$ **do**
7: $y^r \leftarrow 0$
8: $\boldsymbol{FS}^r \leftarrow [\,]$, $\boldsymbol{IrGB}^r \leftarrow [\,]$, and $\boldsymbol{BUFS}^r \leftarrow [\,]$
9: **while** $f \leq |\mathcal{F}|$ & $q < n^r_{\mathrm{FS}}$ & $\mathcal{E}$ **do**
10: $\boldsymbol{FS}^r \leftarrow \mathcal{E}(1 : n^r_{\mathrm{FS}})$, $y^r \leftarrow 1$
11: $q \leftarrow (q + (|\mathcal{M}| \times \Delta_{\mathrm{FS}}))$, $f \leftarrow (f + \Delta_{FS})$
12: **if** $f < |\mathcal{F}|$ & $q > n^r_{\mathrm{FS}}$ & $\mathcal{G}$ **then**
13: $\boldsymbol{BUFS}^r \leftarrow \mathcal{E}((n^r_{\mathrm{FS}} + 1) : |\mathcal{E}|)$, $\boldsymbol{IrGB}^r \leftarrow \mathcal{G}$
14: **else if** $f < |\mathcal{F}|$ & $q == n^r_{\mathrm{FS}}$ & $\mathcal{G}$ **then**
15: $\boldsymbol{IrGB}^r \leftarrow \mathcal{G}$
16: **else if** $f == |\mathcal{F}|$ & $q > n^r_{\mathrm{FS}}$ **then**
17: $\boldsymbol{BUFS}^r \leftarrow \mathcal{E}((n^r_{\mathrm{FS}} + 1) : |\mathcal{E}|)$
18: **else**
19: $q \leftarrow 0$
20: $f \leftarrow f + 1$
$c \leftarrow c + 1$
21: **return** $\boldsymbol{FS}^r$, $\boldsymbol{IrGB}^r$,$\boldsymbol{BUFS}^r$,y^r

ate nodes of each lightpath, i.e., spatial continuity. Therefore, we can drop the super-script l in the allocated FSs, IrGBs, and BUFSs matrices and simply write $\boldsymbol{FS}^{r}$, $\boldsymbol{IrGB}^{r}$, and $\boldsymbol{BUFS}^{r}$. For example, the corresponding matrices for connection 4 in Fig.1 are $\boldsymbol{FS}^4 = \begin{bmatrix} 2 & 3 & 2 \\ 1 & 4 & 2 \\ 2 & 4 & 2 \end{bmatrix}$, $\boldsymbol{IrGB}^4 = \begin{bmatrix} 1 & 5 & 2 \\ 2 & 5 & 2 \end{bmatrix}$, and $\boldsymbol{BUFS}^4 = \begin{bmatrix} 1 & 3 & 2 \end{bmatrix}$.

Furthermore, to satisfy the spectral and spatial continuity condition, the path state tensor ($\boldsymbol{PST}^{r,k} = [\pi^{T^s,r,k}]_{|\mathcal{M}|\times|\mathcal{F}|\times|\mathcal{C}|}$) must be formed. To do this, we find the common idle FSs in all links of the selected path by applying line 3 in Algorithm 1, where operator $\circledast$ is defined as in Eq. (6). Additionally, as shown in Fig.4, the operator $\circledast$ is applied on the same FSs of each core and mode in all links of a path.

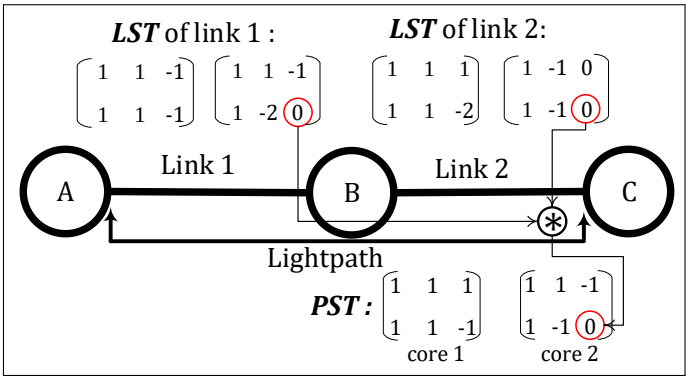

Fig. 4. Illustrative example to denote the function of operator $\circledast$. In this example $|\mathcal{M}| = 2, |\mathcal{F}| = 3$, and $|\mathcal{C}| = 2$. Each row corresponds to a mode, each column corresponds to a frequency, and each matrix corresponds to a core.

$$\pi^{T^s,r,k} = \omega^{T^s,r,l} \circledast \omega^{T^s,r',l'} = \begin{cases} 0 \;; & \text{if } \omega^{T^s,r,l} \text{ and } \omega^{T^s,r',l'} = 0, \\ 1 \;; & \text{if } \omega^{T^s,r,l} \text{ or } \omega^{T^s,r',l'} = 1, \\ -1; & \text{Otherwise .} \end{cases} \tag{6}$$

In Algorithm 1, we define three conditional sets i.e., $\mathcal{A} \equiv \{\pi^{T^s,r,k} \leq 0; \forall m \in |\mathcal{M}| \text{ and } \forall f \in [f, f + \Delta_{\mathrm{FS}} - 1]\}$, $\mathcal{B} \equiv \{\pi^{T^s,r,k} == 0;$ if any $m \in |\mathcal{M}|$ and $\forall f \in [f, f + \Delta_{\mathrm{FS}} - 1]\}$, and $\mathcal{D} \equiv \{\pi^{T^s,r,k} == 0; \forall f \in [f, f + \Delta_{\mathrm{FS}} - 1]\}$. In this algorithm, after each edge FS (unless the edge FS number is $|\mathcal{F}|$) we consider the next FS to be an IrGB. Finally, in line 11 in Algorithm 1, the $T^s|_{f+\Delta_{\mathrm{FS}}} = (m, f + \Delta_{\mathrm{FS}}, c)$. The outputs of Algorithm 1 are the FS, GB, and BUFS matrices and y^r. If $y^r = 1$, the 3DRA was performed successfully, and the connection r can be established. If it is zero, the connection is blocked on the corresponding route, and we must consider other routes.

With respect to conservative 3DRA, we propose Algorithm 2 called CONSERVATIVE function. In addition to the variables and parameters of Algorithm 1, we define two other conditional sets in Algorithm 2, i.e., $\mathcal{E} \equiv \{\pi^{T^s,r,k} == 0; \forall m \in \mathcal{M}$ & $\forall f \in [f, f + \Delta_{\mathrm{FS}} - 1]\}$,$\mathcal{G} \equiv \{\pi^{T^s,r,k} == 0; \forall m \in \mathcal{M}$ & $\forall f \in [f, f + \Delta_{\mathrm{FS}}]\}$.

In Fig.5, we present a simple example to illustrate the difference between the LIBERAL and CONSERVATIVE functions. In this figure, we assume 3 modes, 6 FSs, 2 cores, and 6 connection requests (numbered 1 to 6) with the required number of FSs being 3, 4, 5, 2, 6, and 4, respectively. For simplicity, we assume one FS is required for each Sb-Ch. As shown in Fig.5, the main difference between functions LIBERAL and CONSERVATIVE is related to the insertion of IrGBs and BUFSs. In LIBERAL, it is possible that an FS can serve as a BUFS or an IrGB, depending on the other connections established. In CONSERVATIVE, the BUFSs and IrGBs are explicitly allocated based on each individual connection. For example, in LIBERAL, the FSs labeled $-1/-2$ (i.e., -1 or -2) are the edge FSs that can serve as IrGBs or BUFSs depending on the relative holding times of connections 2 and 3, 4 and 5, and 5 and 6. For example, if connection 4 is torn

Core	Mode	Frequency Slot					
		1	2	3	4	5	6
1	1	11	-1	21	24	-1/-2	33
	2	12	-1	22	-1/-2	31	34
	3	13	-1	23	-1/-2	32	35
2	1	41	-1/-2	52	55	-1/-2	62
	2	42	-1/-2	53	56	-1/-2	63
	3	-1/-2	51	54	-1/-2	61	64

(a) Liberal 3DRA

Core	Mode	Frequency Slot					
		1	2	3	4	5	6
1	1	11	-1	21	24	-1	0
	2	12	-1	22	-2	-1	0
	3	13	-1	23	-2	-1	0
2	1	31	34	-1	41	-1	0
	2	32	35	-1	42	-1	0
	3	33	-2	-1	-2	-1	0

(b) Conservative 3DRA

Fig. 5. First fit MMSC-CFM example comparing the liberal and conservative 3DRA algorithms. Label descriptions are provided in the caption of Fig.3.

down before connection 5, then the FS between 41 and 52 and the FS between 42 and 53 are connection 5's BUFSs and the FS below 42 is an IrGB for connection 5. However, in conservative 3DRA, all IrGBs and BUFSs are designated based on each individual connection, and when the connection is torn down, all corresponding busy FSs are released. Thus, in CONSERVATIVE, holding time plays no role in whether an FS is an IrGB or a BUFS. However, to accomplish this, we must insert an explicit IrGB after the edge FSs and BUFSs. This leads to greater inefficiency, as illustrated in Fig.5 where connections 5 and 6 cannot be established in the conservative approach. Further comparisons of the liberal and conservative approaches are provided in Section 5.

C. Node Architecture

To have a cognitive 3D SDM-FON in which the modulation level can be adapted on-line based on the QoT, we must consider SDN-enabled transceivers and ROADMs (see Fig.6).

As shown in Fig.6, a connection enters via the client ports, and then enters programmable and sliceable flexible OTN interfaces through a flow distributor to construct an OTN frame, i.e., an optical transport unit (OTU) such as OTU-1,2,3,4, and OTU-flex. Next, the essential operations such as encoding, bit-to-symbol mapping, modulation, pulse shaping, digital pre-compensation / pre-distortion are performed in the programmable digital signal processors (P-DSP). For more details, see [38]. Finally, as in [28], the Sb-Chs map to an SSSp-Ch by utilizing programmable BVTs (P-BVTs) and WSSs in SBVTs, mode division multiplexers (MDMs), and fan-in/-out to enter the FM-MCF.

4. DYNAMIC 3D-QOT-AWARE RMRA

Similar to most dynamic RSSA algorithms [17], our proposed dynamic 3D-QoT-aware RMRA is performed in four successive steps: 1) path QoT computation (PQC), 2) dominant path selection (DPS), 3) modulation level selection (MLS), and 4) 3DRA.

We previously discussed the first-fit MMSC-CFM 3DRA scheme, along with the conservative and liberal approaches. Here, we focus on our proposed approaches regarding modulation level, and path selection algorithms that incorporate QoT computation.

A. On-Line vs. Off-Line Modulation Level Selection (MLS)

Each candidate path is associated with a baseline modulation format, based on the distance of the path and the expected QoT. In general, the most bandwidth-efficient modulation format is selected as the baseline. In our proposed on-line MLS algorithm, if the baseline modulation format is no longer feasible due to the current network conditions, then we consider less efficient modulation formats (i.e., lower modulation levels). In contrast, in the off-line MLS algorithm, the modulation format of the candidate path cannot be changed. If it is no longer feasible due to an unacceptable QoT, then the connection is blocked.

With ultra-high bit rate traffic (e.g., 1000 Gbps and beyond), there are numerous Sb-Chs aggregated to create an SSSp-Ch. Selecting a modulation format for each Sb-Ch would present scalability issues. To improve the scalability of our approach, we assume that all Sb-Chs composing a given SSSp-Ch are assigned the same modulation format. This is a reasonable assumption, give that all of the composite Sb-Chs have the same endpoints.

B. Pre-QC vs. Post-QC Path QoT Computation

We introduce two dynamic 3D-QoT-aware RMRA algorithms, namely pre-QC and post-QC. According to Algorithm 3 called PRE-QC, after the candidate route identification steps, we calculate the QoT of all K candidate paths before applying path selection. In contrast, in the post-QC algorithm (Algorithm 4), the QoT calculation is performed for each candidate path one by one. Only if a candidate path is not selected do we need to calculate the QoT for the next candidate path. Thus, we expect that the computation complexity of pre-QC is higher than for post-QC because we typically will perform more QoT calculations in the former. More details on the comparison of these path computation algorithms are provided in Section 5.

In post-QC, if $y^r = 1$, the 3DRA is successful and connection r can be established. Otherwise, the corresponding route is not feasible for this connection and we must continue to consider other routes. In pre-QC, If $\boldsymbol{P}^r \neq [\,]$ (i.e., empty matrix), the 3DRA is successful. If not, the connection is blocked. (In Algorithm 3 and 4, q and $Q_{\text{th}}^{Y^r}$ are a counter and QoT threshold for connection r with modulation level Y^r, respectively.)

C. Dominant Path Selection (DPS) Algorithms

We focus on three dominant path selection (DPS) algorithms, namely shortest path first (SPF), traffic load balancing first (TLBF), and QoT first (QoTF). (Note that the candidate paths are generated using a K-shortest path algorithm.) In previous work [39], we introduced the QoTF DPS algorithm; here, we compare it with the proposed SPF and TLBF algorithms. The QoTF DPS algorithm is only feasible for the pre-QC algorithm; the corresponding strategy to select one of the K candidate paths is (in order of priority): maximum OSNR, minimum modulation level, minimum distance, and maximum TLB factor. In the SPF DPS algorithm, the selection priority is minimum distance and maximum TLB factor. Finally, for TLBF, the selection priority order is maximum TLB and minimum distance. The TLB factor is defined as $\eta_{\text{TLB}}^k = \frac{N_{\text{IFS}}^k}{(d^k)^2}$, where, N_{IFS}^k and d^k is the number of idle FSs and distance (km) of route p^k, respectively. (Note, while

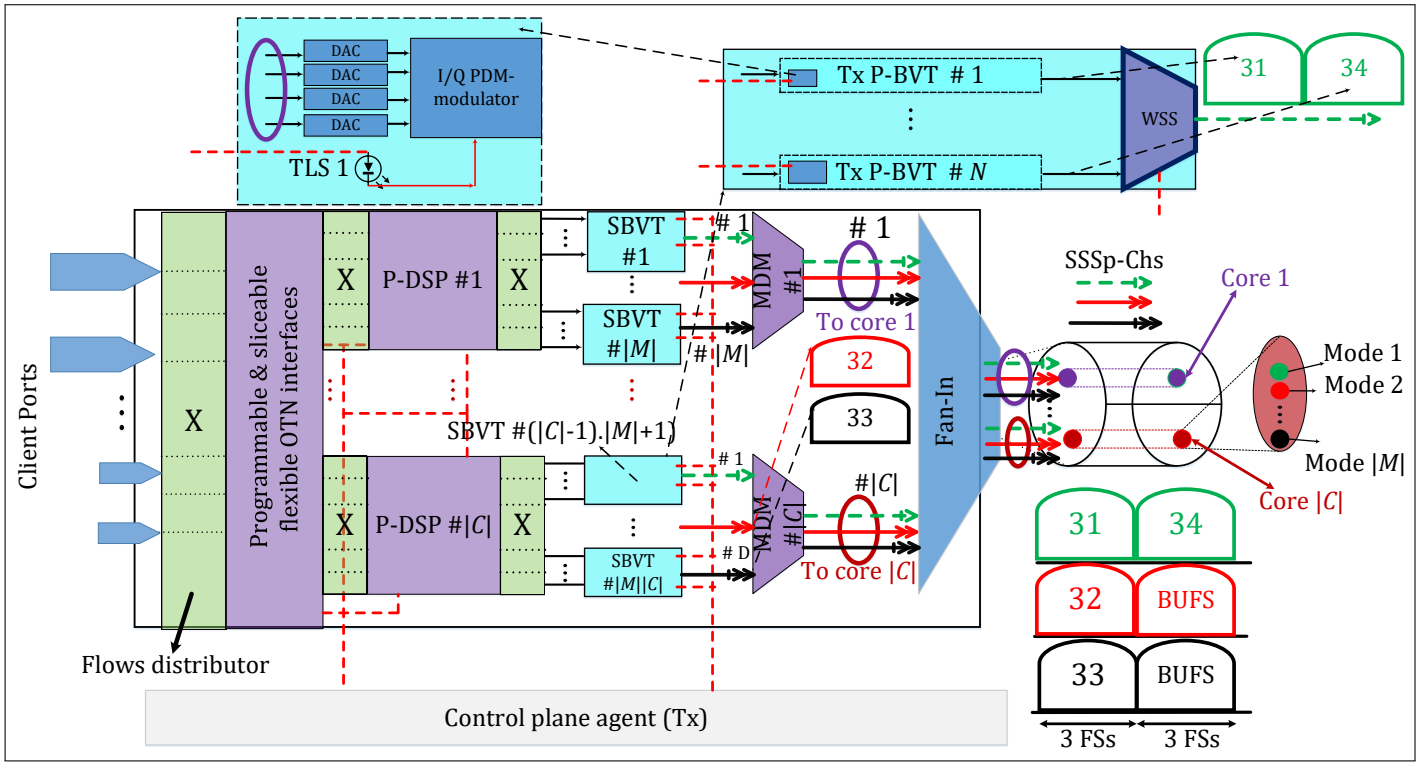

Fig. 6. An architecture of an SDN-controlled transceiver to form a SSSp-Ch in a QoT-aware SDM-FON over FM-MCF. The allocated Sb-Chs for connection 3 with MMSC from Fig.3 are depicted. P-BVT: programmable bandwidth variable transponder, TLS: tunable laser source, DSP: digital signal processor, MDM: mode division multiplexer, WSS: wavelength selective switch, DAC: digital-to-analog converter; PDM: polarization division multiplexer. Only the Tx is shown for simplicity.

the number of hops in a path will affect the number of ROADMs optically bypassed and thus the QoT, we did not incorporate minimizing hops into the path selection strategy.)

It is important to note that we utilize the worst-case constrained XT-aware approach [17] in which we assume the FSs will eventually be fully loaded. With this worst-case assumption, when new connections are added, they will not affect already established connections. Note that, in the MLS step, we initially consider the most spectrum efficient modulation level for the connection request according to its reach distance in the PQC step, which is actually an optimistic guess. This guess is to be confirmed by executing the QoT estimator using the actual network conditions. Therefore, even though we are following a worst-case design approach in order not to affect the already established connections, it is possible that the selected path turns out to be infeasible due to the initial optimistic guess. At this stage, if the QoT cannot be satisfied, the MLS step is repeated until a feasible lower modulation level is found. If the algorithm cannot find a feasible modulation level among the available options, then the candidate path must be changed.

Finally, even though only the on-line versions of the RMRA algorithms are described in Algorithms 3 and 4, by eliminating lines 19 and 20 in Algorithm 3 and lines 21 and 22 in Algorithm 4 (these lines pertain to considering lower modulation levels), one can produce the off-line versions of the algorithms.

5. NUMERICAL RESULTS

This section assesses the BP of SDM-FONs over FM-MCFs, taking into account the limitations that IrM-XT, IaM-XT, and IC-XT impose on the reach distance of the optical signals. We start by presenting the details of the simulation setup. Then we present the most interesting findings of the parameters involved in the operation of the proposed dynamic 3D-QoT-aware RMRA.

A. Simulation Environment

A dynamic network environment is simulated in MATLAB to evaluate the proposed 3D-QoT-aware RMRA algorithms. The developed simulator is an event-driven engine equipped with the proposed QoT estimator for FM-MCFs, in which the initial events are arrival and departure times of each connection request. Once a connection (including bit rate, source, and destination) arrival event occurs, the request is handled by using the proposed 3D-QoT-aware-RMRA algorithms. If these algorithms find a path, the LST of each link in the selected lightpath is updated. With each departure event, a connection is terminated, and its allocated resources are released by updating the LST of all relevant links. All executions are performed using a computer with a Core i7 processor at 2.9 GHz, 8 GB installed memory (RAM), and a 64 bit operating system.

To assess the performance of the proposed algorithms, simulations were performed using the well-known JPN network topology [18]. We assume that each connection is established as a unidirectional lightpath. In JPN, the average distance of all possible source-destination pairs, assuming shortest path routing, is 929 km. The candidate paths are generated using a K-shortest path algorithm with K equal to 3. In all simulations, the bit rate of each connection is uniformly distributed within $\{100, 200, 400, 1000\}$ Gbps and the source and destination of the requests are selected randomly among the network nodes. We performed 10 executions for each offered traffic load and report

Algorithm 3. PRE-QC function

procedure PRE-QC ($R^r = \{N_S^r, N_D^r, \rho^r\}$, network topology graph $G = (\mathcal{N}, \mathcal{L})$, and $\boldsymbol{LST}^l; \forall l \in \mathcal{L}$)
  Calculate K-Shortest Path algorithm
  Initializing:
  $k \leftarrow 1$, $\boldsymbol{P}^r \leftarrow [\,]$
  for k in $[1, K]$ **do**
    if $d^k \leq d_{\max}$ **then**
      Calculate Υ^r according to the d^k
      Calculate n_{FS}^r according to the Υ^r
      if $n_{FS}^r \leq$ the total Idle FSs of $\boldsymbol{PST}^{r,k}$ **then**
        Perform 3DRA (LIBERAL or CONSERVATIVE)
        if $y^r == 1$ **then**
          Calculate OSNR for each Sb-Ch, $q \leftarrow 1$
          while $q \leq \Delta_{FS}$, & $y^r == 1$ **do**
            if OSNR in Eq. (1) $\leq Q_{th}^{\Upsilon^r}$ **then**
              $y^r \leftarrow 0$, and **break while**
            $q \leftarrow (q + 1)$
          if $y^r == 1$ **then**
            Insert k in the $\boldsymbol{P}^r$
          else if $\Upsilon^r > 2$ **then**
            $\Upsilon^r \leftarrow \Upsilon^r - 2$, and go to the line 8
  if $\boldsymbol{P}^r == []$ **then**
    return Connection request r will be blocked
  else
    Calculate TLBs for all path/s in $\boldsymbol{P}^r$
    Select the dominant path based on DPS strategy
    return $\boldsymbol{P}^r$, Sb-Chs' OSNRs, Υ^r, and outputs of 3DRA.

Algorithm 4. POST-QC function

procedure POST-QC ($R^r = \{N_S^r, N_D^r, \rho^r\}$, network topology graph $G = (\mathcal{N}, \mathcal{L})$, and $\boldsymbol{LST}^l; \forall l \in \mathcal{L}$)
  $\boldsymbol{P}^r \leftarrow$ Calculate K-Shortest Path algorithm
  Initializing:
  $k \leftarrow 1$
  Calculate TLBs of all path/s
  for k in $[1, K]$ **do**
    Select the dominant path based on DPS
    if $d^k \leq d_{\max}$ **then**
      Calculate Υ^r according to the d^k
      Calculate n_{FS}^r according to the Υ^r
      if $n_{FS}^r \leq$ the total Idle FSs of $\boldsymbol{PST}^{r,k}$ **then**
        Perform 3DRA (LIBERAL or CONSERVATIVE)
        if $y^r == 1$ **then**
          Calculate OSNR for each Sb-Ch, $q \leftarrow 1$
          while $q \leq \Delta_{FS}$, & $y^r == 1$ **do**
            if OSNR in Eq. (1) $\leq Q_{th}^{\Upsilon^r}$ **then**
              $y^r \leftarrow 0$, and **break while**
            $q \leftarrow (q + 1)$
          if $y^r == 1$ **then**
            break for
          else if $\Upsilon^r > 2$ **then**
            $\Upsilon^r \leftarrow \Upsilon^r - 2$, and go to the line 10
    Remove k from the list of K candidate paths
  if $y^r == 0$ **then**
    return Connection request r will be blocked
  else
    return $\boldsymbol{P}^r$, Sb-Chs' OSNRs, Υ^r, and outputs of 3DRA.

an average BP with a standard deviation of $\backsimeq 0.001$. Each data point was obtained by simulating 10^5 connection requests.

We assume an FM-MCF with $|\mathcal{M}| = 3$ and $|\mathcal{C}| = 7$ per link, with physical parameters reported in [40]. A FM-EDFA [7] with noise figure of $n_F = 5.5$ dB to compensate the fiber span loss is used every $L^{l,i} = 100$ km in all links. The fiber loss coefficient and launch power are considered to be 0.21 dB/Km and 6 dBm [20], respectively. The available spectrum per subspace approximately equals 4.43 THz (C-band from $1530 - 1565$ nm) on the ITU-T 12.5-GHz Flexi-grid standard [41]. Thus, 354 FSs (of 12.5-GHz each) exist per subspace.

Moreover, we assume that each connection must use the same core and mode (spatial continuity) through all links of a lightpath. Indeed, for simplicity and to reduce the port count of the switching module and hardware complexity, we do not consider lane changes (core switching) and mode conversion [42]. Moreover, we assume all-optical transmission with spectrum continuity and contiguity. Using the multi-band OFDM multi-layer transport model [25] and the transceiver architecture of Fig.6, then for a connection request r with a ρ^r Gbps bit-rate, the number of required Sb-Chs can be calculated as follows:

$$n_{Sb}^r = \lceil \frac{\rho^r}{\rho^{\Upsilon^r}} \rceil \quad \textbf{(7)}$$

where ρ^{Υ^r} is the Sb-Ch bit rate, which is determined by the selected modulation level. The possible modulation levels follow Ref.[25] where $\Upsilon^r = 2$, 4, 6, and 8 correspond to PDM-BPSK, PDM-QPSK, PDM-8QAM, and PDM-16QAM, respectively. The respective associated parameters are: bit rates of 12.5, 25, 33.3, and 50 Gbps; optical reach of distance 4000, 2000, 750, 400 km; and acceptable SNR thresholds (as reported in [43] of 3.52, 7.03, 17.59, and 32.60 dB). Therefore, based on Eq. (7), we can calculate the number of required FSs of connection r, i.e., n_{FS}^r including the FSs for Sb-Chs, BUFSs, and IrGBs by Eq. (8) and Eq. (9) as follows:

$$B^r = n_{Sb}^r \times B_{Sb} + B_{IrGB}^r + B_{BUFS}^r \quad \textbf{(8)}$$

$$n_{FS}^r = \lceil \frac{B^r}{B_{FS}} \rceil \quad \textbf{(9)}$$

In Eq. (8) and Eq. (9), $B_{Sb} = \Delta_{FS} \times B_{FS}$ and $\lceil \bullet \rceil$ is the ceiling function, and Δ_{FS} is the required number of FSs for each Sb-Ch with channel spacing $B_{FS} = 12.5$ GHz [41]. It should be noted that B^r contains the IaGBs, similar to [25]. For simplicity, we assume that the transceivers operate at a fixed baud rate, i.e., 12 GBaud [25], thus, $\Delta_{FS} = 1$ is fixed for all SBVTs. Furthermore, B_{IrGB} equals 12.5 GHz for each SSSp-Ch in each subspace, and B_{BUFS} equals 12.5 GHz for each BUFS. Finally, B_{IrGB}^r and B_{BUFS}^r can be calculated based on the 3DRA algorithm, with the resulting number of $\boldsymbol{IrGB}^r$ and $\boldsymbol{BUFS}^r$ rows multiplied by B_{FS}, respectively.

Consider an example where $\Delta_{FS} = 1$ and the desired reach and bit rate of the connection request are 900 Km and 90 Gbps, respectively, and the modulation level is selected as PM-QPSK (i.e., $\Upsilon^r = 4$). Then $\rho^{\Upsilon^r} = 25$ Gbps and n_{Sb}^r is calculated to be 4 using Eq. (7).

B. Performance Comparison

As mentioned in Section 4, our proposed 3D-QoT-Aware RMLSAs have four steps, including 3DRA, MLS, PQC, and DPS. We proposed two algorithms for 3DRA (i.e., liberal and conservative), two for MLS (i.e., on-line and off-line), two for PQC (i.e.,

Table 2. Six Studied 3D-QoT-Aware RMRA Scenarios (A-F)

Scenario Name	3DRA	PQC	DPS	MLS
A	Liberal	post-QC	SPF	on-line
B	Conservative	post-QC	SPF	on-line
C	Liberal	post-QC	SPF	off-line
D	Liberal	post-QC	TLBF	on-Line
E	Liberal	pre-QC	QoTF	on-Line
F	Liberal	pre-QC	QoTF	off-Line

post-QC and pre-QC), and three for DPS, i.e., SPF, TLBF, and QoTF. Due to the large number of possible permutations, we have limited our study to the 6 scenarios listed in Table 2, where in each scenario our goal is to minimize BP.

First, we focus on comparing the liberal and conservative 3DRA algorithms by considering scenarios **A** and **B**. In these scenarios the same algorithms are implemented in the PQC, DPS, and MLS steps. Then, we compare on-line and off-line MLS by considering scenarios **A** and **C**. Next, we compare the three DPSs, focusing on scenarios **A**, **D**, and **E**. Finally, we compare pre- and post-QC strategies.

In all six scenarios, the prime metric used to evaluate the performance is the BP in the JPN network, where BP is calculated by $BP = \frac{n_{\mathrm{BL}}}{n_{\mathrm{All}}}$, where n_{BL} and n_{All} are the number of blocked requests and total requests, respectively. Note that BP simply considers the fraction of connection requests that are blocked; it does not take into account the bandwidth of the request. Bandwidth blocking percentage would have been a more informative metric; however, we have assumed that fairness with respect to connection bandwidth among the various studied schemes is approximately the same. This needs to be confirmed in future work.

In the traffic model, we assume Poisson arrivals (with mean χ) and exponential holding times (with parameter ψ). Therefore, $\frac{\psi}{\chi}$ represents the offered traffic load in Erlangs, where it is varied between $[700 - 1100]$ Erlangs by fixing χ at 0.01 and increasing ψ from 7 to 11. The main results are shown in Fig. 7 and Table 3. The rows of this table will be explained below.

B.1. Liberal vs. conservative 3DRA

As stated above, we compare *liberal* and *conservative* 3DRA using scenarios **A** and **B**; the remaining algorithm steps are the same in both of these scenarios.

In Fig.7, we see that the BP of scenario **A** is slightly lower than that of scenario **B**. Adding the top two rows of Table 3, we see that the average occupied spectrum per established connection corresponding to IrGBs and BUFSs is 48.8 GHz using conservative 3DRA and 48.5 GHz for the liberal scheme. Thus, based on these metrics, there is little performance difference between the two schemes. However, a more important difference is that scenario **B** requires on average one fewer laser per established connection. This potentially represents an appreciable cost savings for a network with heavy traffic (especially because the lasers are assumed to be tunable in Fig.6).

In terms of average 3DRA computation time (CT-3DRA) per established connection (i.e., row 4), scenario **B** has a better performance with 0.98 msec, as compared to 1.6 msec for scenario **A**. This is due to scenario **A** requiring that the holding times of

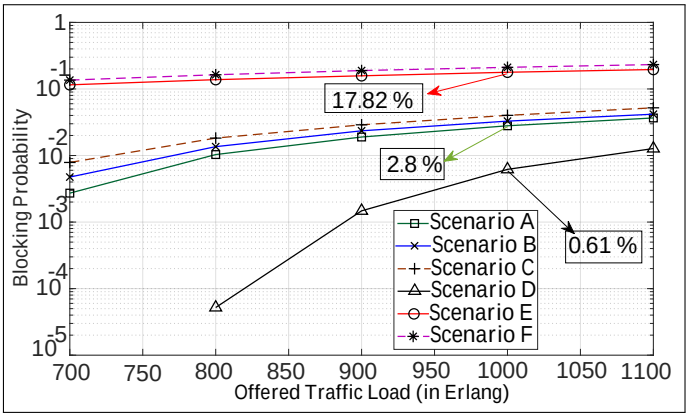

Fig. 7. BP vs. offered traffic load for the six studied RMRA scenarios.

Table 3. Comparison of the six studied RMRA Scenarios in Terms of the Average IrGBs Bandwidth, BUFSs Bandwidth, Computation Time (CT), OSNR, and Modulation Level Change (MLC), where the averages are taken over the range of Offered Traffic Load.

Scenario	**A**	**B**	**C**	**D**	**E**	**F**
IrGBs (GHz)	25.7	37.3	25.0	25.7	25.6	25.0
BUFSs (GHz)	22.8	11.5	24.5	22.9	23.2	24.6
Number of lasers	6	5	6	6	4	5
CT-3DRA (msec)	1.60	0.98	1.50	1.55	2.45	2.13
CT-RMRA (msec)	44.30	40.06	44.50	46.50	55.36	49.43
OSNR(dB)	21.7	22.9	20.8	19.9	22.9	22.0
MLC (%)	18.5	18.6	0	17.2	25.3	0

edge FSs be processed (i.e., because of the FSs that are either IrGBs or BUFSs depending on the established connections). Furthermore, the computation time of the whole 3D QoT-aware RMRA algorithm (i.e., row 5) is 40.1 msec for scenario **B** and 44.3 msec for scenario **A**. (The standard deviations of CT-3DRA and CT-RMRA are on the order of 0.0002 for all scenarios.)

Because of the greater average bandwidth used for guardbands in the conservative 3DRA scenario (i.e., row 1), this results in decreasing IrM- and IaM-XT effects, resulting in a higher average OSNR per established connection (i.e., row 6) in scenario **B** (i.e., 21.7 dB in **A** and 22.9 dB in **B**). Finally, as shown by the last row of Table 3, the adjustment of modulation levels (made possible by the on-line MLS) is approximately the same in both scenario **A** and **B**.

For the remaining scenarios studied here, we only consider the liberal 3DRA algorithm. However, note that we did compare liberal vs. conservative in scenarios not included here, and the same relative behaviors as reported above were exhibited.

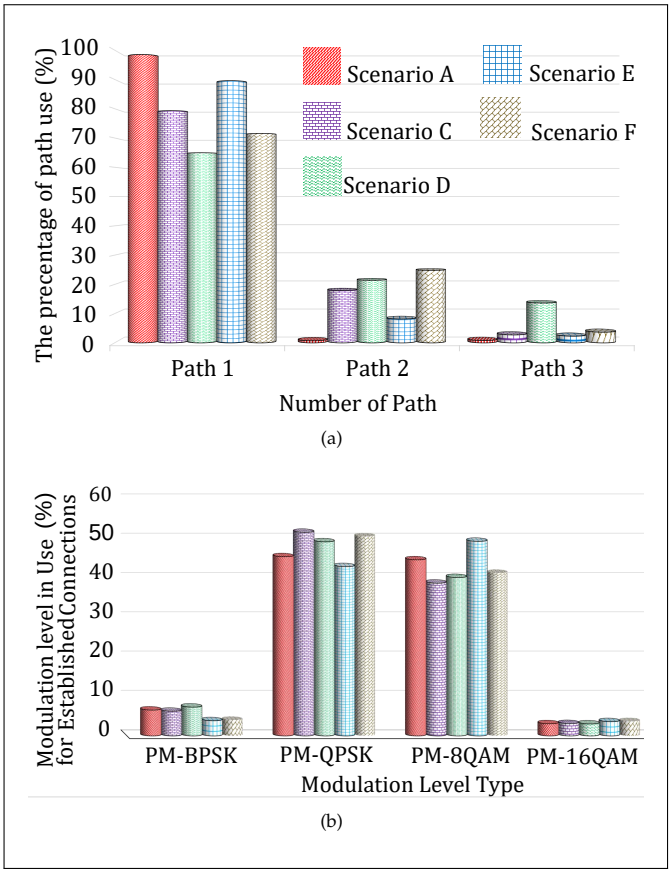

Fig. 8. (a) The percentage of path usage, and (b) The average modulation level usage for liberal pre-QC and post-QC scenarios (for traffic load 700-1100 Erlang in the JPN network.

B.2. On-line vs. off-line MLS

Because scenarios **A** and **C** use the same 3DRA, the values of IrGBs, BUFSs, number of lasers, and CT-3DRA for these two scenarios are very similar. However, as shown in Fig.7, scenario **C** (off-line MLS) results in a slightly higher BP compared with scenario **A** (on-line MLS). This is because the modulation level is fixed for a connection in scenario **C**, whereas scenario **A** can take advantage of adjustable modulation levels. Note that the ability to select the modulation level did not appreciably impact the computation times.

Regarding QoT, the average OSNR of established connections for scenario **A** is slightly higher than that for scenario **C** (21.7 vs 20.8 dB). The main reason is likely related to path selection. Indeed, as shown in Fig.8(a), the off-line MLS algorithm (scenario **C**) uses second and third candidate paths (which are longer than the first shortest path) more often as compared with the on-line MLS algorithm (scenario **A**). These longer paths are expected to have lower OSNR.

Overall, the on-line MLS algorithm increases the QoT while slightly improving the BP in comparison with the off-line MLS algorithm.

B.3. DPS Performance comparison

As shown in Fig.7, the lowest BP is attained in scenario **D**, in which the DPS algorithm is TLBF. For example, the BP is significantly lower than that attained in scenario **A** where SPF is used as the DPS algorithm. There is even a greater improvement as compared to scenario **E** where pre-QC QoTF is utilized as the DSP algorithm. However, the average OSNR attained in scenario **A** and **E** is higher than that in scenario **D** (**A**: 21.7 dB and **E**: 22.9 dB vs. **D**: 19.9 dB). This is due to the second and third candidate paths being used more frequently in scenario **D**, as shown in Fig.8(a). With respect to MLS, we see that the TLBF algorithm reduces the percentage of MLC of the established connections by balancing the traffic among the candidate paths (**A**: 18.5% and **E**: 25.3% vs. **D**: 17.2%).

Overall, the much better BP results favor the use of TLBF.

B.4. Post-QC vs. Pre-QC

We now focus on post-QC vs. pre-QC, where pre-QC is used in conjunction with the QoTF DPS. We focus on comparing the two pre-QC scenarios (**E** and **F**) with the other scenarios, all of which utilize post-QC. Pre-QC yields significantly higher BP than any of the post-QC scenarios. Additionally, as expected, the computation times are longer with pre-QC due to having to evaluate the QoT for all K candidate paths. MLC is noticeably higher in scenario **E**; again, this is due to each candidate path always being evaluated, where MLC can occur with each such evaluation.

There is a moderate improvement in the average OSNR of established connections, especially in **E**. This is related to the path usage, where, as shown in Fig.8(a), the first shortest path is used heavily in scenario **E**; i.e., the second and third shortest paths, which are longer, are not used frequently. It is interesting to note that even though scenario **A** uses the first shortest path more than scenario **E**, it has a lower average OSNR. This may be due to there being so many connections on the shortest path that XT impairments begin to rise, thereby reducing the OSNR.

The one appreciable advantage of pre-QC is exemplified in scenario **E**, where the number of required lasers, i.e., 4, is the lowest among all scenarios.

B.5. Modulation Level Usage

The modulation format affects spectral efficiency and energy consumption [44]. Thus, it is worth considering whether any of the scenarios had an appreciable effect on the choice of modulation level. Given the average path length of 910 km in the JPN network topology, it is expected that PM-QPSK and PM-8QAM would be predominantly used. Indeed, this was borne out, as shown in Fig.8(b). There were only minor differences in modulation level usage among the various scenarios, with scenario **E** taking best advantage of the more efficient PM-8QAM (i.e., more efficient than PM-QPSK).

6. CONCLUSION

In this manuscript, we proposed several dynamic 3D-QoT-aware RMRA algorithms for SDN-enabled SDM-FONs over FM-MCFs. With regard to the physical layer model, we focused on weakly-coupled modes over uncoupled cores according to the GN-model and proposed a closed-form OSNR formula as a QoT estimator. Here, we focused on the multi-mode single-core strategy for distributing the FSs of a connection to sub-channels, with CFM search priority. However other strategies and search priorities may prove to be better depending on factors such as fiber type and impairments.

The main findings of our simulations reveal that: (i) even though the liberal 3DRA has lower BP compare to conservative 3DRA, this difference is not significant. On the other hand, the conservative approach provides benefits in computation time, average OSNR, and number of required lasers, (ii) the on-line

MLS algorithm improves the network performance in terms of BP and the average OSNR of established connections, as compared to off-line MLS; however, the computation time is higher, (iii) the TLBF DPS approach yielded significantly lower blocking, (iv) the QoTF pre-QC algorithm yielded the highest blocking, but somewhat higher average OSNR (v) the on-line algorithm increases the use of higher modulation levels, and finally (vi) the proposed 3DRA and MLS algorithms had a small impact on OSNR and BP, whereas the proposed DPS algorithm had a much larger effect.

REFERENCES

1. C. V. Forecast, "Cisco visual networking index: Forecast and trends, 2017–2022," White paper, Cisco Public Inf. (2019).
2. M. Jinno, "Spatial channel network (SCN): Opportunities and challenges of introducing spatial bypass toward the massive SDM era," J. Opt. Commun. Netw. **11**, 1–14 (2019).
3. M. Klinkowski and K. Walkowiak, "An efficient optimization framework for solving RSSA problems in spectrally and spatially flexible optical networks," IEEE/ACM Transactions on Netw. **27**, 1474–1486 (2019).
4. I. Tomkos, S. Azodolmolky, J. Sole-Pareta, D. Careglio, and E. Palkopoulou, "A tutorial on the flexible optical networking paradigm: State of the art, trends, and research challenges," Proc. IEEE **102**, 1317–1337 (2014).
5. R. Munoz, N. Yoshikane, R. Vilalta, J. M. Fabrega, L. Rodriguez, D. Soma, S. Beppu, S. Sumita, R. Casellas, R. Martinez, T. Tsuritani, and I. Morita, "Adaptive software defined networking control of space division multiplexing super-channels exploiting the spatial-mode dimension," IEEE/OSA J. Opt. Commun. Netw. **12**, A58–A69 (2020).
6. M. Habibi and H. Beyranvand, "Impairment-aware manycast routing, modulation level, and spectrum assignment in elastic optical networks," IEEE/OSA J. Opt. Commun. Netw. **11**, 179–189 (2019).
7. T. Mizuno, H. Takara, K. Shibahara, A. Sano, and Y. Miyamoto, "Dense space division multiplexed transmission over multicore and multimode fiber for long-haul transport systems," J. Light. Technol. **34**, 1484–1493 (2016).
8. N.-P. Diamantopoulos, B. Shariati, and I. Tomkos, "On the power consumption of MIMO processing and its impact on the performance of SDM networks," in *2017 Optical Fiber Communications Conference (OFC),* (IEEE, 2017), pp. 1–3.
9. R. Rumipamba-Zambrano, J. Perelló, and S. Spadaro, "Route, modulation format, MIMO, and spectrum assignment in flex-grid/MCF transparent optical core networks," J. Light. Technol. **36**, 3534–3546 (2018).
10. I. Sartzetakis, K. Christodoulopoulos, and E. Varvarigos, "Cross-layer adaptive elastic optical networks," J. Opt. Commun. Netw. **10**, A154–A164 (2018).
11. E. E. Moghaddam, H. Beyranvand, and J. A. Salehi, "Routing, spectrum and modulation level assignment, and scheduling in survivable elastic optical networks supporting multi-class traffic," J. Light. Technol. **36**, 5451–5461 (2018).
12. D. Klonidis, F. Cugini, O. Gerstel, M. Jinno, V. Lopez, E. Palkopoulou, M. Sekiya, D. Siracusa, G. Thouénon, and C. Betoule, "Spectrally and spatially flexible optical network planning and operations," IEEE Commun. Mag. **53**, 69–78 (2015).
13. A. Muhammad, G. Zervas, and R. Forchheimer, "Resource allocation for space-division multiplexing: Optical white box versus optical black box networking," J. Light. Technol. **33**, 4928–4941 (2015).
14. M. Yaghubi-Namaad, A. G. Rahbar, and B. Alizadeh, "Adaptive modulation and flexible resource allocation in space-division-multiplexed elastic optical networks," J. Opt. Commun. Netw. **10**, 240–251 (2018).
15. M. Yaghubi-Namaad, A. G. Rahbar, B. Alizadeh, and A. Ghadesi, "Switching adaptable optimization of resource allocation for space division multiplexed elastic optical networks," Opt. Switch. Netw. **31**, 8–21 (2019).
16. E. E. Moghaddam, H. Beyranvand, and J. A. Salehi, "Crosstalk-aware resource allocation in survivable space-division-multiplexed elastic optical networks supporting hybrid dedicated and shared path protection," J. Light. Technol. **38**, 1095–1102 (2020).
17. M. Klinkowski, P. Lechowicz, and K. Walkowiak, "Survey of resource allocation schemes and algorithms in spectrally-spatially flexible optical networking," Opt. Switch. Netw. **27**, 58–78 (2018).
18. H. Tode and Y. Hirota, "Routing, spectrum, and core and/or mode assignment on space-division multiplexing optical networks," J. Opt. Commun. Netw. **9**, A99–A113 (2017).
19. Q. Yao, H. Yang, R. Zhu, A. Yu, W. Bai, Y. Tan, J. Zhang, and H. Xiao, "Core, mode, and spectrum assignment based on machine learning in space division multiplexing elastic optical networks," IEEE Access **6**, 15898–15907 (2018).
20. F. Arpanaei, B. Shariati, N. Ardalani, H. Beyranvand, and A. Alavian, "Physical-layer aware routing, modulation level and resource allocation of SDM networks over FM-MCFs," in *proceeding of ECOC 2019; presented at 45th European Conference on Optical Communication (ECOC),* (Dublin, Sep, 2019), p. 4 pp.
21. M. Cvijetic, I. B. Djordjevic, and N. Cvijetic, "Dynamic multidimensional optical networking based on spatial and spectral processing," Opt. express **20**, 9144–9150 (2012).
22. F. Arpanaei, N. Ardalani, H. Beyranvand, and S. A. Alavian, "Three-dimensional resource allocation in space division multiplexing elastic optical networks," J. Opt. Commun. Netw. **10**, 959–974 (2018).
23. R. Muñoz, N. Yoshikane, J. M. Fàbrega, L. Rodríguez, R. Vilalta, D. Soma, S. Beppu, S. Sumita, R. Casellas, R. Martínez, T. Tsuritani, and I. Morita, "SDN-enabled scaling up/down of sdm super-channels exploiting spatial modes with adaptive mimo equalization and modulation format assignment," in *Optical Fiber Communication Conference (OFC) 2019,* (Optical Society of America, 2019), p. M4J.7.
24. P. S. Khodashenas, J. M. Rivas-Moscoso, D. Siracusa, F. Pederzolli, B. Shariati, D. Klonidis, E. Salvadori, and I. Tomkos, "Comparison of spectral and spatial super-channel allocation schemes for SDM networks," J. Light. Technol. **34**, 2710–2716 (2016).
25. E. Pincemin, M. Song, J. Karaki, O. Zia-Chahabi, T. Guillossou, D. Grot, G. Thouenon, C. Betoule, R. Clavier, A. Poudoulec, M. Van der Keur, Y. Jaouën, R. Le Bidan, T. Le Gall, P. Gravey, M. Morvan, B. Dumas-Feris, M. L. Moulinard, and G. Froc, "Multi-Band OFDM transmission at 100 Gbps with sub-band optical switching," J. Light. Technol. **32**, 2202–2219 (2014).
26. M. Song, E. Pincemin, A. Josten, B. Baeuerle, D. Hillerkuss, J. Leuthold, R. Rudnick, D. M. Marom, S. Ben Ezra, J. F. Ferran, G. Thouenon, P. S. Khodashenas, J. M. Rivas-Moscoso, C. Betoule, D. Klonidis, and I. Tomkos, "Flexible optical cross-connects for high bit rate elastic photonic transport networks [invited]," IEEE/OSA J. Opt. Commun. Netw. **8**, A126–A140 (2016).
27. Y. Mori, K. Yamashita, and M. Jinno, "Feasibility demonstration of integrated fractioanal joint switching WSS applicable for few-mode multicore fiber," in *2018 Photonics in Switching and Computing (PSC),* (IEEE, 2018), pp. 1–3.
28. R. Muñoz, N. Yoshikane, R. Vilalta, J. M. Fàbrega, L. Rodríguez, R. Casellas, D. M. S. Moreolo, R. Martínez, L. Nadal, D. Soma, Y. Wakayama, S. Beppu, S. Sumita, T. Tsuritani, and I. Morita, "SDN control of sliceable multidimensional (spectral and spatial) transceivers with YANG/NETCONF," IEEE/OSA J. Opt. Commun. Netw. **11**, A123–A133 (2019).
29. T. Hayashi, T. Nagashima, K. Yonezawa, Y. Wakayama, D. Soma, K. Igarashi, T. Tsuritani, and T. Sasaki, "6-mode 19-core fiber for weakly-coupled mode-multiplexed transmission over uncoupled cores," in *Optical Fiber Communications Conference (OFC), 2016,* (IEEE, 2016), pp. 1–3.
30. S. Mumtaz, R.-J. Essiambre, and G. P. Agrawal, "Nonlinear propagation in multimode and multicore fibers: generalization of the Manakov equations," J. Light. Technol. **31**, 398–406 (2012).
31. T. Hayashi, T. Taru, O. Shimakawa, T. Sasaki, and E. Sasaoka, "Uncoupled multi-core fiber enhancing signal-to-noise ratio," Opt. express **20**, B94–B103 (2012).
32. B. Li, L. Gan, S. Fu, Z. Xu, M. Tang, W. Tong, and P. P. Shum, "The role of effective area in the design of weakly coupled MCF: Optimiza-

tion guidance and OSNR improvement," IEEE J. Sel. Top. Quantum Electron. **22**, 81–87 (2015).
33. B. Shariati, A. Mastropaolo, N.-P. Diamantopoulos, J. M. Rivas-Moscoso, D. Klonidis, and I. Tomkos, "Physical-layer-aware performance evaluation of SDM networks based on SMF bundles, MCFs, and FMFs," J. Opt. Commun. Netw. **10**, 712–722 (2018).
34. A. E. Elfiqi, A. A. Ali, Z. A. El-Sahn, K. Kato, and H. M. Shalaby, "Theoretical analysis of long-haul systems adopting mode-division multiplexing," Opt. Commun. **445**, 10–18 (2019).
35. P. Poggiolini, G. Bosco, A. Carena, R. Cigliutti, V. Curri, F. Forghieri, R. Pastorelli, and S. Piciaccia, "The LOGON strategy for low-complexity control plane implementation in new-generation flexible networks," in *2013 Optical Fiber Communication Conference (OFC),* (IEEE, 2013), pp. 1–3.
36. A. Mirani, H. Beyranvand, and J. A. Salehi, "Analytical derivation of channel capacity in uncompensated optical space-division multiplexing systems," in *2017 Iran Workshop on Communication and Information Theory (IWCIT),* (2017), pp. 1–6.
37. M. Klinkowski and K. Walkowiak, "Impact of crosstalk estimation methods on the performance of spectrally and spatially flexible optical networks," in *2018 20th International Conference on Transparent Optical Networks (ICTON),* (IEEE, 2018), pp. 1–4.
38. N. Sambo, P. Castoldi, A. D'Errico, E. Riccardi, A. Pagano, M. S. Moreolo, J. M. Fàbrega, D. Rafique, A. Napoli, S. Frigerio, E. H. Salas, G. Zervas, M. Nolle, J. K. Fischer, A. Lord, and J. P. F. . Giménez, "Next generation sliceable bandwidth variable transponders," IEEE Commun. Mag. **53**, 163–171 (2015).
39. H. Beyranvand and J. A. Salehi, "A quality-of-transmission aware dynamic routing and spectrum assignment scheme for future elastic optical networks," J. Light. Technol. **31**, 3043–3054 (2013).
40. Y. Sasaki, Y. Amma, K. Takenaga, S. Matsuo, K. Saitoh, and M. Koshiba, "Trench-assisted low-crosstalk few-mode multicore fiber," in *39th European Conference on Optical Communication (ECOC 2013),* (IET, 2013), pp. 1–3.
41. G. Recommendation, "694.1: Spectral grids for WDM applications: DWDM frequency grid," Int. Telecommun. Union, Tech. Rep (2012).
42. B. Shariati, J. M. Rivas-Moscoso, D. M. Marom, S. Ben-Ezra, D. Klonidis, L. Velasco, and I. Tomkos, "Impact of spatial and spectral granularity on the performance of SDM networks based on spatial superchannel switching," J. Light. Technol. **35**, 2559–2568 (2017).
43. L. Yan, E. Agrell, H. Wymeersch, and M. Brandt-Pearce, "Resource allocation for flexible-grid optical networks with nonlinear channel model," J. Opt. Commun. Netw. **7**, B101–B108 (2015).
44. B. S. G. Pillai, B. Sedighi, K. Guan, N. P. Anthapadmanabhan, W. Shieh, K. J. Hinton, and R. S. Tucker, "End-to-end energy modeling and analysis of long-haul coherent transmission systems," J. Light. Technol. **32**, 3093–3111 (2014).